Ultramicroscopy 203 (2019) 105–118

Contents lists available at ScienceDirect

Ultramicroscopy

journal homepage: www.elsevier.com/locate/ultramic

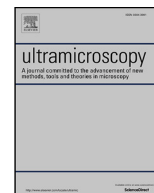

Quantitative measurement of nanoscale electrostatic potentials and charges using off-axis electron holography: Developments and opportunities☆

Martha R. McCartney[a,*], Rafal E. Dunin-Borkowski[b], David J. Smith[a]

[a] Department of Physics, Arizona State University, Tempe, AZ 85287, USA

[b] Ernst Ruska-Centre for Microscopy and Spectroscopy with Electrons and Peter Grünberg Institute, Forschungszentrum Jülich, 52425 Jülich, Germany

ARTICLE INFO

Keywords:
Phase imaging
Polarization fields
Fringing fields
Electrical biasing
Off-axis electron holography
Electrostatic potentials

ABSTRACT

Off-axis electron holography has evolved into a powerful electron-microscopy-based technique for characterizing electromagnetic fields with nanometer-scale resolution. In this paper, we present a review of the application of off-axis electron holography to the quantitative measurement of electrostatic potentials and charge density distributions. We begin with a short overview of the theoretical and experimental basis of the technique. Practical aspects of phase imaging, sample preparation and microscope operation are outlined briefly. Applications of off-axis electron holography to a wide range of materials are then described in more detail. Finally, challenges and future opportunities for electron holography investigations of electrostatic fields and charge density distributions are presented.

1. Introduction

The technique of electron holography was originally proposed by Gabor as a strategy for overcoming the fundamental barrier to electron microscope resolution arising from spherical aberration [1]. However, its practical implementation in the transmission electron microscope (TEM) was delayed until the development of the high-brightness, field-emission electron gun (FEG), which provides the required highly coherent illumination [2]. Most modern high-resolution and analytical TEMs are equipped with FEGs, facilitating the development and application of electron holography and related techniques. The TEM mode of off-axis electron holography is by far the most common of the many possible variants of electron holography [3], and it was the approach used by Lichte and his colleagues in some of the first convincing demonstrations of aberration correction using the technique [4]. Significant improvements in spatial resolution using electron holography, as well as convenience in operation, have also resulted from the introduction of microscope hardware for aberration correction [5]. Since a reconstructed electron hologram provides access to the phase of the electron wavefunction after it has passed through a thin, electron-transparent specimen, off-axis holography enables electromagnetic fields to be characterized and quantified with high spatial resolution and sensitivity [6].

This review focuses on the use of off-axis electron holography to achieve quantitative mapping of electrostatic potentials and measurements of electrostatic fields and charge density distributions. We begin with a short synopsis of the theoretical basis of the technique and experimental considerations, including essential aspects of microscope operation and sample preparation. Important developments in the study of electrostatic fields, including recent and emerging applications, are then described, with an emphasis on quantitative measurements. The final section presents ongoing challenges, which result from reduced sample dimensions, sample charging and electrostatic fringing fields, and discusses future opportunities, such as *in situ* experiments and electron holographic tomography. The interested reader is also referred to additional review papers for further information about the development and applications of electron holography and related techniques [6–14, 130–132].

2. Basis of off-axis electron holography

Changes in the phase of the incident electron beam caused by electrostatic potentials within and surrounding a TEM specimen are not directly observable in conventional electron micrographs, which typically contain only intensity information. Electron holography enables this limitation to be overcome, as demonstrated in Fig. 1, which shows: a) an experimental off-axis electron hologram of a doped Si-Ge nanowire; and b) a color-coded representation of the corresponding

☆ This paper is dedicated to Professor Hannes Lichte on the occasion of his 75th birthday.

* Corresponding author.
E-mail address: molly.mccartney@asu.edu (M.R. McCartney).

https://doi.org/10.1016/j.ultramic.2019.01.008
Received 30 November 2018; Received in revised form 27 December 2018; Accepted 21 January 2019
Available online 10 February 2019
0304-3991/ © 2019 Elsevier B.V. All rights reserved.

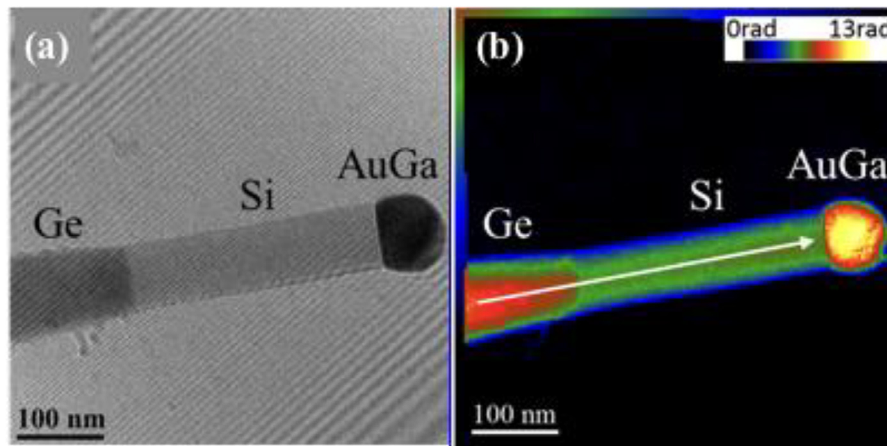

Fig. 1. (a) Off-axis electron hologram of a doped Ge-Si NW with a AuGa growth catalyst particle; (b) Corresponding reconstructed phase image visualized with pseudo-color. Color scale at top right.

reconstructed phase *change* of the electron beam across the field of view. Subsequent analysis and interpretation of this phase image can be used to obtain quantitative information about the projected electrostatic potential distribution. Electric fields and charge density distributions can also be quantified, subject to certain requirements and limitations that are described below.

The region of interest on the specimen is normally positioned so that it covers approximately half of the field of view. An electrostatic biprism, which takes the form of a thin (< ~1 µm diameter) wire [15], is usually located for convenience in place of one of the selected-area apertures. The application of a voltage to the biprism results in overlap of a vacuum reference wave with the electron wave that has passed through the specimen, as shown schematically in Fig. 2. Holographic interference fringes are formed in the overlap region if the electron illumination is sufficiently coherent. The contrast of the interference fringes is proportional to the amplitude of the electron wavefunction that reaches the detector, while the desired phase information is encoded in their relative positions. Since a vacuum reference wave needs to be overlapped with the area of interest on the specimen, it is helpful for many applications if the edge of the specimen is visible within the field of view of the phase image. The phase offset in vacuum (or in a thin and weakly scattering underlying support film) can then be assigned to a value of zero. In addition to the coherent FEG electron source and post-specimen electrostatic biprism, a recording device with high dynamic range and excellent input-output linearity, such as a charge-coupled-device (CCD) camera or a direct electron detector, is essential for achieving quantitative amplitude and phase measurements using electron holography, as illustrated in Fig. 3. By recording the interference pattern (i.e., hologram) in digital form, rapid retrieval and reconstruction of the complex electron wavefunction is greatly facilitated. Additional post-specimen lenses, such as a mini-(Lorentz) lens in the bore of the lower objective lens polepiece, are also useful for providing increased imaging flexibility in terms of the accessible ranges of magnification, interference fringe spacing and overlap width.

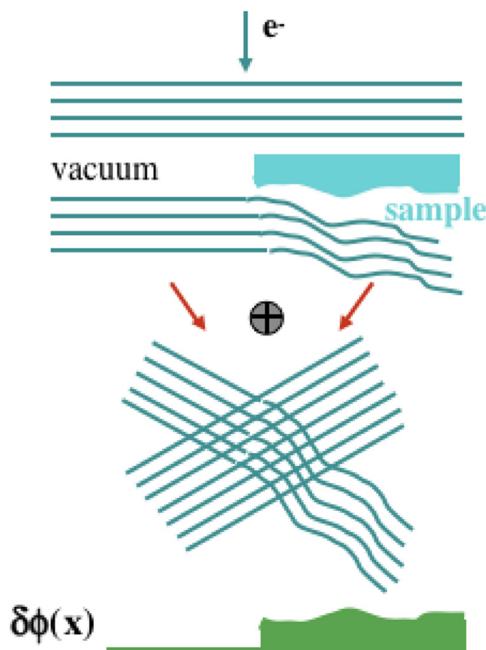

Fig. 2. Sketch illustrating the origin of phase shifts in an electron-transparent specimen relative to a vacuum (or reference) wave, which are used for the quantification of electrostatic fields using the technique of off-axis electron holography.

If the effects of dynamical electron diffraction are neglected (i.e., if the specimen is treated as thin and weakly diffracting), then the phase change of the electron wave transmitted by the object relative to that of the vacuum or reference wave is given (in one dimension) by the expression

$$\delta\phi(x) = C_E \int V(x, z)dz - \frac{e}{\hbar} \int\int B_{\perp}(x, z)dx\, dz \tag{1}$$

where z is the incident electron beam direction, x is a direction in the plane of the specimen, V is the total electrostatic potential within and around the specimen, and $B_{\perp}$ is the component of magnetic induction perpendicular to the electron beam direction [16]. C_E is an interaction constant that depends on the energy of the incident electron beam and is given by the expression

$$C_E = \frac{2\pi}{\lambda E}\frac{E + E_0}{2E + E_0} \tag{2}$$

where λ is the wavelength and E and E_0 are the kinetic and rest mass energies, respectively, of the incident electron beam. C_E takes a value of 0.00653 rad/(V.nm) at a microscope accelerating voltage of 300 kV. Since electromagnetic fields that are outside the specimen, including fringing fields originating from other microscope components, can influence the phase change that is finally recorded, Eq. (1) should in principle be evaluated along the entire path of the electron wave from the FEG electron source to the detector. Moreover, crystalline materials should be tilted away from zone-axis orientations. If long-range electrostatic (or magnetic) fringing fields that originate from charges (or magnetic moments) in the sample only perturb the reference wave that is used to form the electron hologram slightly, then their presence can

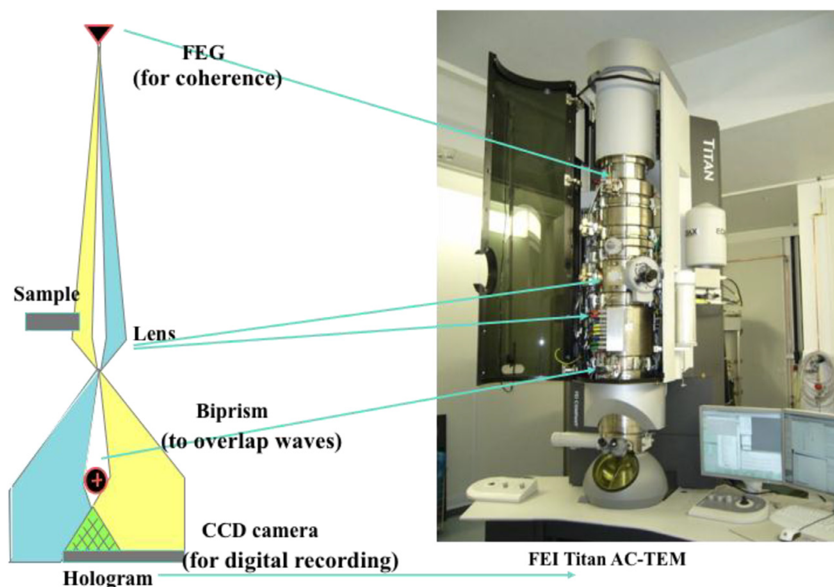

Fig. 3. (Left) Sketch indicating the microscope components that are essential for off-axis electron holography: (i) the field-emission gun (FEG) provides coherent incident illumination; (ii) the electrostatic biprism provides overlap of object and vacuum reference waves; and (iii) the CCD camera enables quantitative electron hologram recording. A Lorentz mini-lens provides additional flexibility by enabling observations to be made with a much larger field of view. (Right) Photograph of a FEI Titan 80-300 aberration-corrected transmission electron microscope equipped for off-axis electron holography experiments.

be taken into account simply by flattening the phase in vacuum. However, if they affect the reference wave strongly, then they may need to be simulated computationally to remove their contributions to the phase shift in the region of interest Because of the non-uniformity of fields along the electron beam direction for specimens such as charged nanowires, it may sometimes be necessary to carry out tomographic holography in order to determine the full three-dimensional electrostatic potential distribution associated with the sample [17].

In many practical cases, V and B are approximately constant within the sample thickness t, and there are no significant electrostatic and/or magnetic fringing fields outside the sample. Eq. (1) can then be simplified in one dimension to

$$\delta\phi(x) = C_E V(x)t(x) - \frac{e}{\hbar}\int B_\perp(x)t(x)dx \tag{3}$$

For the non-magnetic materials that are considered in the present paper, the second term in Eq. (3) is zero. The final simplified expression includes contributions to the electrostatic potential from both local variations in the mean inner potential (MIP) (*i.e.*, the composition and density) of the specimen and longer-range charge redistribution. A recorded phase image therefore provides the basis for the measurement and quantification of electrostatic fields in many practical situations, as explained below. Prior knowledge of the local value of the MIP, which is usually written V_0, is often crucial for quantifying the electrostatic potential distribution. However, calculations based on neutral atom scattering factors tend to overestimate V_0 [18], highlighting the need for experimental measurements of this key parameter [19]. Measurements of V_0 usually require an independent estimate of the specimen thickness profile. In addition, it is essential to minimize dynamical diffraction effects by avoiding zone axes and other strongly diffracting orientations. A convenient table listing MIP values for many common materials has been published [18]. Further discussions about the measurement and calculation of the MIP can be found elsewhere [e.g., 14].

The local variation in electrostatic potential associated with the presence of a *p-n* junction in a doped semiconductor device consists of two primary terms: the MIP of the sample V_0 and the built-in junction potential, which is commonly written V_{bi}. The phase change can then be written in the form

$$\delta\phi(x) = C_E[V_0(x) + V_{bi}(x)]t(x). \tag{4}$$

Quantification of the junction potential ideally requires information about the MIP and/or the local specimen thickness. Convergent beam electron diffraction with a probe size of ~2–10 nm is well suited for determining the local thickness of a crystalline sample with an accuracy of ~5% over the thickness range that is appropriate for off-axis electron holography [19]. The measured MIP of crystalline Si based on using this approach is 12.0 ± 0.2 V [19], while its value is 14.0 ± 0.6 V for crystalline GaAs [20]. Alternatively, the local specimen thickness can be determined from an amplitude image if independent prior knowledge of the inelastic mean free path is available [21].

After digital recording of the electron hologram, which consists of interference fringes that are modulated in phase and amplitude by the fields within and surrounding the object, image processing can be used to reconstruct the (complex) wavefunction. The phase shifts caused by the specimen can then be extracted and quantified. Fig. 4 illustrates this reconstruction procedure for a doped Si nanowire. Fig. 4(a) shows the original electron hologram, while Fig. 4(b) shows an enlargement of the hologram that illustrates local bending of the interference fringes caused by the presence of the nanowire. The Fast Fourier Transform of the hologram shown in Fig. 4(c) has a central auto-correlation peak, as well as two sidebands, which contain the desired phase information. Fig. 4(d) shows the reconstructed complex image wave, obtained by masking one of the sidebands, centering it in Fourier space, and then applying an Inverse Fourier Transform. Fig. 4(e) shows the final phase image, which is obtained by evaluating the arctangent of the ratio of the imaginary and real parts of the complex image wave. The projected electrostatic potential (and/or the projected in-plane magnetic field) within and surrounding the sample can then be inferred by taking factors such as the specimen composition and thickness into account. Computer programs that are suitable for these processing steps have been developed by several investigators, and are also commercially available. It is even possible to carry out hologram reconstruction in real time at the microscope at rates of up to several frames per second, rather than waiting until after the microscope session is completed.

3. Practical aspects

3.1. Phase imaging

The electrostatic biprism is key to phase imaging using off-axis electron holography, since it enables interference of the object and reference waves to produce an electron hologram. The biprism must be able to sustain potentials as high as 1000 V for atomic-resolution studies [22]. Quartz fibers coated with very thin metallic films are most commonly used, but Pt wires are also supplied by one microscope

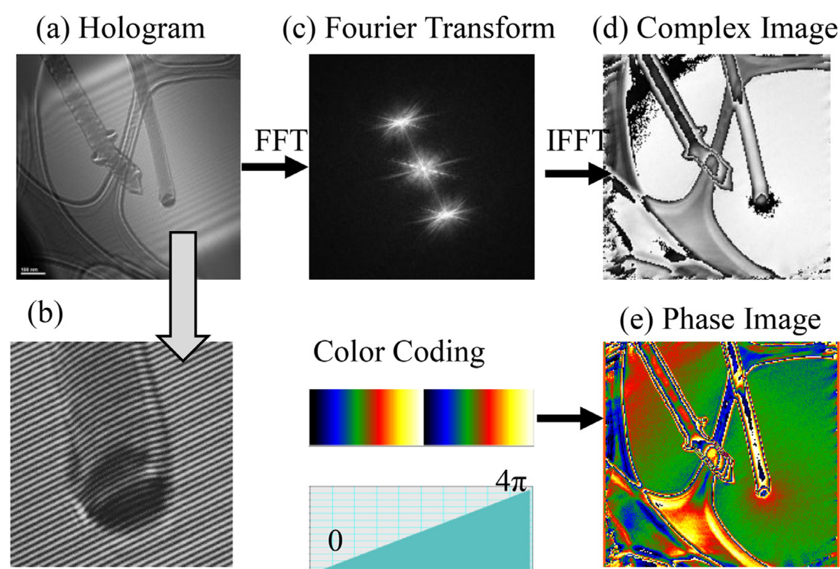

Fig. 4. Sequence of steps that are involved in quantitative phase imaging using the technique of off-axis electron holography. (a) Off-axis electron hologram showing doped Si NW supported on holey C film; (b) Enlargement showing bending of holographic interference fringes at the edges of Si NW; (c) Fast Fourier Transform (FFT) of hologram; (d) Reconstructed complex image calculated by Inverse Fourier Transformation of one of the sidebands in the FFT; (e) Color-coded phase image showing projected electrostatic potential across field of view.

manufacturer. The wire should preferably be rotatable, so that it can be aligned with specimen features of interest. It should also be mechanically stable to avoid drift or vibrations that could reduce interference fringe contrast and degrade the final phase image. It is therefore usually preferable to align the biprism so that it is normal to the long axis of the aperture holder.

The bias voltage applied to the biprism determines several important, inter-related parameters: the spacing and contrast of the interference fringes and the extent of the fringe overlap region, which is often termed the overlap width. Initially, with no voltage applied to the biprism, Fresnel diffraction fringes outline the shadow of the biprism wire. As the applied voltage is increased, the electron waves on each side of the wire start to overlap, producing relatively coarse interference fringes that are still affected by Fresnel diffraction from the edges of the wire. The fringe spacing and contrast both decrease upon increasing the voltage further, while the overlap width increases. Fresnel diffraction effects are then only visible at the edges of the overlap region. Higher applied voltages can be used to expand the field of view further and to produce finer interference fringe spacings, which should in principle result in better spatial resolution in reconstructed phase images. However, these gains are also accompanied by a decrease in fringe contrast, which has a negative impact on image quality due to poorer signal-to-noise in the final phase image. A compromise in terms of fringe spacing and minimum usable fringe contrast eventually needs to be made, which depends on the particular microscope and the specific application.

The interference fringe spacing varies inversely with biprism voltage, as well as with electron energy, objective lens focal length, and the location of the biprism in the microscope column [23]. Although calculation of the fringe spacing is possible when the relevant microscope dimensions are known, it is simpler to make experimental measurements for a specific microscope geometry, as shown in Fig. 5(a). Similarly, it is straightforward to measure and plot the width of the fringe overlap region as a function of biprism voltage, as shown in Fig. 5(b). The contrast (i.e., visibility) of the interference fringes ultimately determines the precision of a phase measurement [24]. It is therefore essential to avoid or at least minimize contributing factors that have negative effects, including mechanical and electrical instabilities, incident beam energy spread, and external stray magnetic fields [25]. The fringe contrast can be written in the form

$$\Gamma = \frac{I_{\max} - I_{\min}}{I_{\max} + I_{\min}} \tag{5}$$

where I_{max} and I_{min} are measured directly from an electron hologram recorded under stable conditions with the sample removed from the field of view.

It is also necessary to consider the interplay between spatial resolution, magnification, fringe spacing and detector pixel size, as discussed in detail elsewhere [23]. Undersampling of the interference fringes on a CCD camera may cause a dramatic decrease in fringe contrast by factors of 3 or more [26], or they may even be completely destroyed. The effect can be avoided, or at least minimized, by using a sufficiently high image magnification. In our experience, when studying nanoscale fields, the interference fringe spacing should preferably be approximately one third of the targeted spatial resolution in the phase image. However, increased sampling may be desirable for samples with atomic-resolution detail, so that the sidebands are well separated from the central maximum and diffraction spots. Moreover, for studies that require sensitive phase measurements, the image magnification should ideally be adjusted so that each fringe period is sampled by at least 6, and preferably as many as 10, detector pixels. These requirements can be relaxed somewhat when using the latest generation of electron detectors, which have improved point spread functions and better detection quantum efficiencies.

3.2. Guidelines for operation

Off-axis electron holography sessions usually begin with a short period when the electron microscope is operated in its normal imaging mode. Standard alignment of the incident beam illumination is made, any required specimen tilting is carried out, and the image astigmatism is corrected. The specimen feature of interest is located and brought into focus. It should also be confirmed that the edge of the specimen, whose location is important for the formation of the vacuum reference wave, will remain in the field of view when electron holography observations begin.

Additional practical factors need to be considered. For example, effects that are not associated with genuine specimen features, such as electron-beam-induced charging, projector lens distortions, and nonlinearities of the detector, can perturb the phase information about the specimen that is contained in the displaced hologram fringes. It is therefore standard practice to record a reference electron hologram with the specimen removed from the field of view, without making any other changes to the microscope imaging parameters. Phase images that are (almost) free of distortions and artefacts can then be obtained by carrying out a complex division of the object and reference waves,

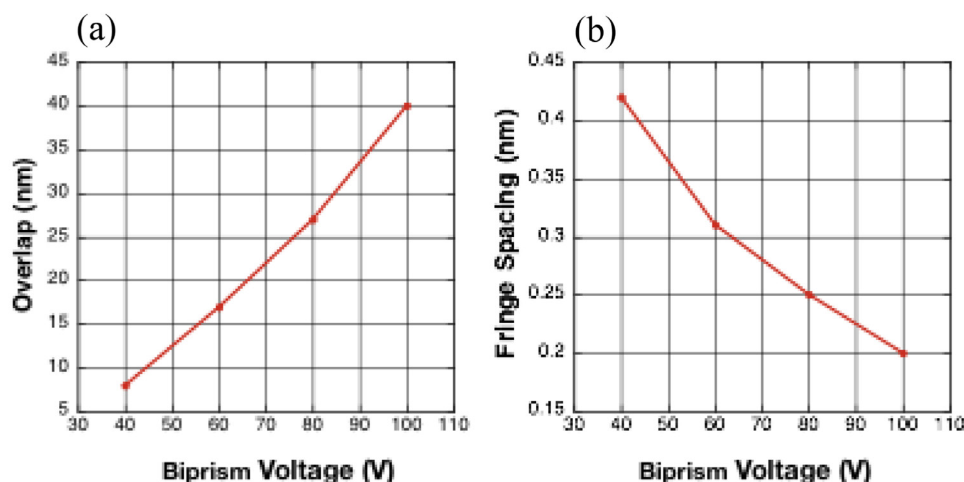

Fig. 5. (a) Line profile showing the increase of the overlap width of an off-axis electron hologram with biprism voltage for a Philips CM200-FEG TEM operated at 200 kV. (b) Line profile showing the dependence of holographic interference fringe spacing on applied biprism voltage for a Philips CM200-FEG TEM operated at 200 kV.

before evaluating the phase of the resulting wavefunction [24].

The coherence of the electron beam incident on the sample, as determined by the effective source size, is a crucial instrumental parameter because it determines the contrast (*i.e.*, visibility) of the holographic interference fringes. Unlike conventional TEM imaging, where rotationally symmetric illumination is normally used, highly elliptical illumination is often implemented for electron holography. This configuration provides a significant gain in lateral beam coherence for a given hologram acquisition time, even for high-brightness field-emission electron sources. This ellipticity is achieved by adjusting the condenser lens stigmators, so that the area illuminated in the specimen plane is very wide in a direction perpendicular to the biprism wire, but narrow in the orthogonal direction parallel to the biprism wire, with the condenser lens overfocused. Typically, the minor axis should be 2–5 times larger than the region of overlap between the object and reference waves, while the major axis should be 50–100 times larger [26]. The beam coherence should be maximized to the greatest possible extent by orienting the elongated beam to be perpendicular to the direction of the biprism wire.

3.3. Sample preparation

The minimization of artifacts due to sample preparation is an important aspect of making reliable measurements of electrostatic potentials and charge density distributions using off-axis electron holography, especially in the case of semiconducting materials and devices. The area intended for examination needs to be electron-transparent and close to the specimen edge in order to ensure the availability of a reference wave. A specimen such as a semiconductor device should often be prepared with uniform thickness, or with a well-defined thickness profile, in order to improve the accuracy of interpretation of the reconstructed phase image. In this respect, wedge polishing is very useful for the preparation of such TEM specimens [27]. Misleading phase shifts due to diffraction effects or bend contours can be minimized by tilting the sample away from a zone-axis orientation [28]. However, some compromise in the amount of tilt may be needed to avoid smearing out interface profiles in nanostructured devices [29]. Sample charging due to the electron-beam-induced emission of secondary electrons can degrade measurements of electrostatic potential [30], and can sometimes be reduced by coating the sample surfaces with C before commencing electron holography studies [19].

Recognizing and avoiding sample preparation artifacts represents an ongoing concern for quantitative electron holography studies. Mechanical polishing followed by Ar ion milling at low energy is a common method used for preparing cross-sectional specimens of materials such as semiconductors [31]. However, early off-axis electron holography studies of Si *p-n* junctions showed that Ar ion milling could give rise to amorphous layers that are up to 25 nm in thickness on both sample surfaces, as well as to additional crystalline regions of the specimen that are electrically inactive [32]. Low angle wedge polishing followed by low angle, low energy ion milling and coating with a thin C film has been shown to mitigate such effects [19], and high quality potential maps of field effect transistors prepared using this method have been reported [27].

Different approaches for sample thinning are required when the device region or feature of interest is located well below the sample surface. Focused-ion-beam (FIB) milling has developed into a site-specific, analytical tool that is now widely used for TEM specimen preparation, for example in the semiconductor industry for failure analysis [33]. However, FIB milling of Si-based specimens can result in the formation of electrically inactive surface layers that have thicknesses as high as ~100 nm for typical dopant concentrations [34], as a result of the penetration of Ga ions deep into the sidewalls of the material [35]. Early electron holography studies of doped Si devices were focused on removing the effects of electrically inactive surface layers from electrostatic potential measurements by recording changes in potential as a function of specimen thickness in wedge-shaped samples that had been prepared using FIB milling [36, 37].

Strategies for minimizing FIB-induced artifacts include *in situ* electrical biasing [38], *in situ* annealing [39], and low-energy backside ion milling [40]. Uneven milling of wafers can create specimen thickness corrugations, which are commonly referred to as "curtaining" [34]. This type of sample artifact has been shown to be alleviated by "backside" FIB milling, as well as by completing the thinning process using gentle, low-angle milling in a conventional Ar ion mill [41]. A discussion of FIB milling of semiconductors, and suggestions for viable strategies that can be used to minimize artifacts in holographic phase images, can be found elsewhere [42]. Since the latest generation of FIB systems allows final milling to be performed at energies of 500 eV or even lower, some of these problems for semiconductor devices are now markedly reduced.

4. Measurement of electrostatic potentials and charge density distributions

This section provides examples of the application of off-axis electron holography to the measurement and quantification of electrostatic fields and charge density distributions in materials that are of scientific interest and technological importance. These studies highlight the usefulness of off-axis electron holography for determining important material parameters that are not accessible using other techniques.

4.1. Dopant profiles and p-n junctions

The mapping of dopant distributions in semiconductor devices with

nanometer spatial resolution is an all-important task for the electronics industry. Device behavior is determined directly by local variations in internal electrostatic potential associated with the presence of dopants. These variations in potential can be complicated, especially for nanostructured devices in which lateral diffusion can occur as a result of device processing [43]. Secondary-ion mass spectrometry can be used to measure dopant concentrations to better than the part per million level, but its lateral resolution is inherently limited [44]. Dopant distributions are not measured directly using off-axis electron holography. Instead, the technique provides measurements of projected electrostatic potential, which are then interpretable in terms of the dopant distribution, with a spatial resolution that is currently inaccessible using other techniques. Many electron holography studies of doped semiconductors have been published. The following examples constitute a representative selection that charts progress in this field. Examples of studies of doped nanowires and electrical biasing experiments involving doped materials are described below in Sections 4.4 and 4.6, respectively.

Both sample preparation and electron microscope technology limited early pioneering electron holography studies of doped semiconductors [45, 46]. Later device studies made use of digital recording and more flexible electron optics, such as the availability of an additional mini-lens for optimizing the magnification between the sample and the biprism. It was established that the *internal* variation in electrostatic potential across an unbiased Si *p-n* junction due to a simple one-dimensional (1D) dopant profile could be mapped and quantified with nanoscale resolution [47]. Subsequent studies of a wedge-polished, C-coated sample demonstrated a spatial resolution of ~5 nm and a sensitivity of ~ 0.1 V [48]. Spatial resolutions of better than 10 nm with a sensitivity of 0.1 V were demonstrated for two-dimensional (2D) mapping of electrostatic potentials associated with metal-oxide-semiconductor (MOS) transistors [32]. Comparisons between experimental and simulated 2D potential profiles were then performed with a spatial resolution of ~6 nm and a sensitivity of ~0.17 V for a *p*-doped field effect transistor, as shown in Fig. 6 [43]. Comparable results in terms of spatial resolution were also reported for other Si-based devices (see, for example, [49–52]).

More recent device studies have provided further improvements in spatial resolution and/or sensitivity. Measurements of a 90-nm Si *p*-channel device were reported with experimental uncertainties of ± 0.1 V in electrostatic potential and ± 3 nm in spatial dimension [27], and a scaled MOSFET with a gate length of only 30 nm was also investigated [52] Observations of Si test samples with precisely controlled doping layers, which took advantage of an aberration-corrected TEM with exceptional mechanical stability, demonstrated that steps in

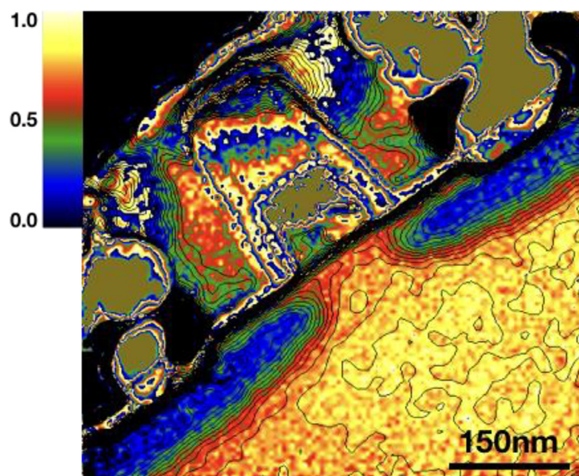

Fig. 6. Reconstructed phase image showing electrostatic potential variations associated with a 0.13 µm *p*-FET semiconductor device. Reprinted from [43].

electrostatic potential as small as 0.030 ± 0.003 V could be measured [25]. An electron holographic tomography approach was used to visualize the three-dimensional (3D) electrostatic potential distribution associated with an electrically biased Si *p-n* junction in a FIB-prepared TEM specimen [53]. This study revealed an extensive region of dopant deactivation in the near-surface regions of the specimen, which was attributable to the FIB milling that had been used for sample preparation. Even larger thicknesses of electrically inactive surface layers were reported for FIB-milled GaAs *p-n* junctions. Substantial reductions in electrically inactive layer thickness from 80 to 17 nm were then achieved by using *in situ* annealing [54]. The use of *in situ* electrical biasing was also reported to contribute to the recovery of the expected built-in junction potential [39]. Additional electrical biasing studies of doped semiconductor devices are described below in Section 4.6. Further challenges and opportunities associated with studying deep-sub-micron-sized electronic device structures using off-axis electron holography have been discussed elsewhere (e.g., [55–60]).

4.2. Quantum dots and charged defects

Charge accumulation can occur at quantum dots (QDs) and structural defects such as dislocations. However, accurate quantification of the amount of charge and the local charge density distribution using off-axis electron holography can be difficult to achieve because of overlap effects in the electron beam direction, the influence of the high energy electron beam on the charge density distribution in the specimen, and stringent sample preparation requirements. Nevertheless, the technique has been used successfully to determine the presence and amount of charge within suitably thinned specimens. The accumulation of positive charge (i.e., holes) in individual Ge QDs was identified [61]. The samples in this study had to be prepared using wedge polishing, since ion implantation and any non-uniformities in sample thickness had to be avoided. Self-assembled Ge QDs were sandwiched between B-doped Si layers, resulting in the formation of valence-band offsets and hole confinement in the QDs. The shapes of the QDs and the amount of Si above and below each QD in the electron-beam direction had to be taken into account. Simulations based on a 1D form of the Poisson equation were used to interpret the projected electrostatic potential in terms of the amount of accumulated charge. The number of holes per unit volume was estimated to be ~30 ± 3 holes/QD, which was close to the average number of 40 holes per Ge QD measured using a macroscopic capacitance-voltage method. In a similar study, electric fields across individual wurtzite GaN QDs embedded in AlN were found to be as high as 7.8 MV/cm, as shown in Fig. 7, in agreement with atomistic tight binding calculations [62]. The sample geometry in this investigation was especially challenging, because the GaN QDs were enclosed entirely in the AlN matrix. Separate MIP contributions to the phase from the different materials, which overlapped along the electron beam direction, had to be considered.

The study of charged defects such as dislocations using electron holography is even more challenging than the quantification of charge in QDs. In addition to demanding sample preparation, effects such as structural disorder, impurity segregation and strong dynamical diffraction are possible. Electron holography studies of undoped GaN indicated that edge, mixed and screw dislocations were negatively charged [63]. In a similar study, dislocations in *n*-GaN were reported to be negatively charged [64]. Cross-sectional studies of dislocations in *n*-ZnO revealed the presence of negative charge near the defect cores, with charge densities of ~2 electrons/nm [65, 66]. Studies of threading screw dislocations in *n*-doped 4H-SiC reported the presence of negatively charged dislocation cores, with comparisons between experiments and simulations showing that the density of trapped charges correlated with the doping level [67]. For a specific sample geometry, the possibility of counting the amount of charge on an individual nanoparticle with a sensitivity of one elementary unit of charge has been demonstrated [68].

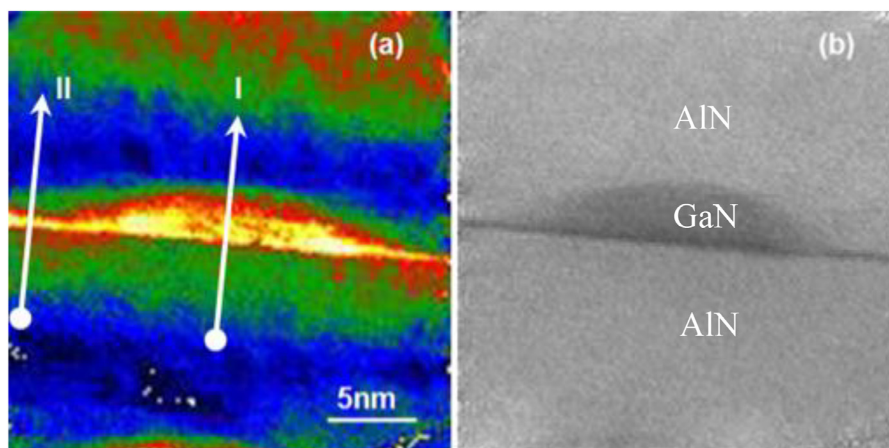

Fig. 7. (a) Phase and (b) amplitude images calculated from an off-axis electron hologram of a wurtzite GaN QD embedded in an AlN matrix. The amplitude image was needed to distinguish between the AlN and GaN MIP contributions to the phase. Reprinted from [62].

4.3. Polarization charge and interfacial sheet charge

Electrostatic fields and sheet charge distributions in III-nitride semiconductors have been investigated extensively using off-axis electron holography [69]. These materials contain high polarization fields as a result of their polar nature, leading to charge accumulation at internal interfaces. Studies of GaN/InGaN/GaN quantum wells (QWs), which are of interest for applications in light-emitting diodes, have indicated the presence of interfacial sheet charge and piezoelectric fields of up to ~4 MV/cm [70, 71], while a 2D electron gas (2DEG) was reported in the vicinity of a GaN/AlGaN heterointerface [72]. An interfacial bound sheet charge density of $8.5 \times 10^{12}/cm^2$ was reported for an AlGaN/AlN/GaN heterostructure [73], whereas a 2DEG of $\sim 2.1 \times 10^{13}/cm^2$ was required to explain an experimental potential profile for the more complicated case of a *p*-AlGaN/InGaN/*n*-AlGaN light-emitting diode structure [74]. In single InGaN/GaN QWs, it was confirmed that the electric field strength varied with In content in the wells [75]. Studies of $In_{0.13}Ga_{0.87}N$ QWs as a function of layer thickness showed that the average electrostatic fields were as high as 1.7 MV/cm across thinner QWs, but that the field strengths decreased for higher well thicknesses [76]. Electric fields as high as 1.28 MV/cm were measured across 6-nm-thick QWs in AlGaN/GaN QW structures [77], and a 2DEG of $6.4 \times 10^{13}/cm^2$ was reported for a *p*-type AlGaN/AlN/GaN heterostructure [78]. Detailed electron holography studies were performed on polarization fields and sheet charge densities in AlInN/AlN/GaN heterostructures, which are of interest for applications in high electron mobility transistors [79]. In this work, a potential profile measured from a phase image, which is shown in Fig. 8, corresponded to an electric field strength of ~6.9 MV/cm, which was consistent with theoretical calculations. Moreover, the positive curvature in a phase profile measured from the GaN layer near the AlN/GaN interface was indicative of the presence of a 2DEG. Further curve fitting and analysis indicated that the integrated 2DEG density was $\sim 2.1 \times 10^{13}/cm^2$. Electrostatic potential profiles have been measured across one-monolayer-thick InN/GaN multiple QWs [80]. The electric fields inside the GaN barriers were found to decrease from ~0.7 MV/cm to ~0.2 MV/cm as the layer thickness increased from 5 to 20 nm, in agreement with computer simulations that predicted a red shift in the photoluminescence peak with increasing thickness of the GaN barrier layer [80].

4.4. Nanowires and nanotubes

A fruitful area for electron holography studies that has experienced increased activity in recent years is the investigation of electrostatic potential distributions associated with nanowires (NWs) and nanotubes. Early examples included the mapping of charge density distributions in Si NWs [81] and core-shell NWs consisting of doped Ge shells surrounding intrinsic Ge cores [82]. In a study of Ge-Si core-shell NWs, off-axis electron holography was used to quantify hole accumulation in the core regions of undoped Ge-Si core-shell NWs resulting from valence band offsets between the materials [83]. Holography studies showed that axial *p*-n junctions in GaAs NWs had built-in potentials of 1.5 ± 0.1 V [84]. Observations of axial *p-n* junctions in Si NWs, as illustrated in Fig. 9, showed potential profiles with heights of 1.0 ± 0.3 V, while comparisons with device simulations indicated dopant concentrations of $\sim 10^{19}/cm^2$ for donors and $\sim 10^{17}/cm^2$ for acceptors [85]. In this work, difficulties were experienced with charging of the Au catalyst particles at the ends of the NWs. More consistent junction profiles were obtained by coating the samples with C before observation. Further analysis revealed that the NWs had equiphase or equipotential surfaces across the *p-n* junction, meaning that the surface potential was pinned mid-gap, while comparisons with simulations enabled the Schottky barrier height and the active dopant concentrations to be estimated [85]. Observations of axial *p-n* heterojunctions in P-doped Si/B-doped Ge NWs proved to be more complicated due to NW kinking near the junctions. The average built-in potential was measured to be ~0.6 V, which was slightly higher than the expected value of 0.4 V [86]. Electron holography studies have been applied to a Schottky barrier formed by a Au catalyst particle at the tip of a NW [85, 87]. Further experiments and simulations are needed to improve measurement accuracy and to investigate the role of experimental and material parameters, such as the work functions of the Au catalyst particles that cap the NWs [86].

Off-axis electron holography has been used to evaluate active dopant distributions in GaP NWs with radial core-shell *p-n* junctions formed using different precursors during growth [88]. Similarly, electrostatic potential distributions have been investigated across radial *p-i-n* structures in patterned arrays of GaAs nanowires for solar cell applications [89]. Attention has also been directed towards studies of nanoscale electrostatic fields produced by polarization-induced charge redistribution at homogeneous zincblende (ZB)/wurtzite (WZ) heterojunctions in InAs(Sb) nanopillars [90], and ZnSe nanobelts [91]. Finally, 3D electrostatic potential mapping of NWs has been achieved by using electron holographic tomography. This technique has been applied to the examination of GaAs-AlGaAs core-shell NWs [92] and an *n*-type MOSFET device [93, 94]. Subsequent experiments combined this approach with annular dark-field STEM tomography to distinguish between local variations in chemical composition and space charge [95].

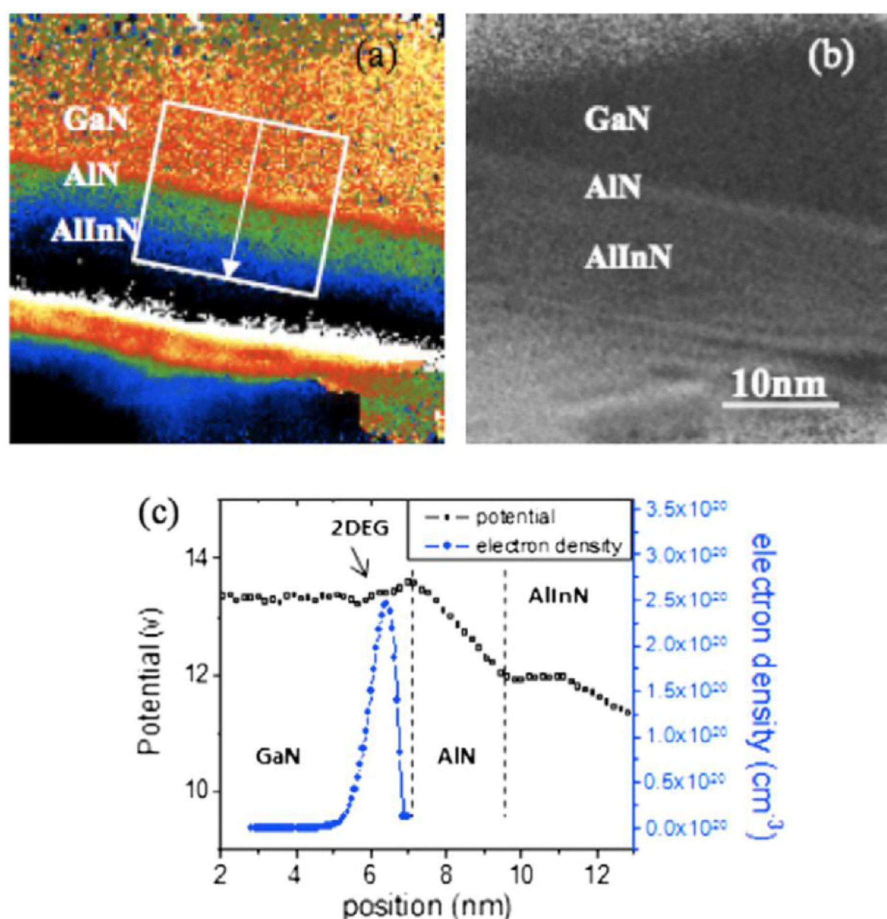

Fig. 8. (a) Reconstructed phase image of an $Al_{0.85}In_{0.15}N$/AlN/GaN high electron mobility transistor; (b) Phase image across the AlInN/AlN/GaN interface region; (c) Potential profile (open squares) and inferred electron distribution (filled circles) across the AlInN/AlN/GaN interface. Reprinted from [79].

4.5. Electrostatic fringing fields

Electrostatic fields that extend outside the surface of a specimen into vacuum have been studied using off-axis electron holography. Such fields are difficult to measure because of their inherently 3D nature. The vacuum reference wave may then be perturbed by the long-range electrostatic fringing field of the specimen, and modeling combined with simulations is often required to achieve satisfactory quantification. Early electron holography observations were performed on electrostatic fringing fields outside electrically biased W microtips [96], as well as on pairs of parallel 1-µm-diameter Pt wires held at different potentials [97] and single conducting wires [98]. Subsequently, off-axis electron holography was used to map electrostatic potentials around the ends of C nanotubes that were electrically biased to study the effects of field emission on external fields [99]. Electron holography observations of electrostatic fringing fields were reported for $TaSi_2$ nanowires [100], cone-shaped C nanotips [101, 102], and atom probe needles [103, 104]. Fig. 10 shows results from a study of C-cone field-emitting

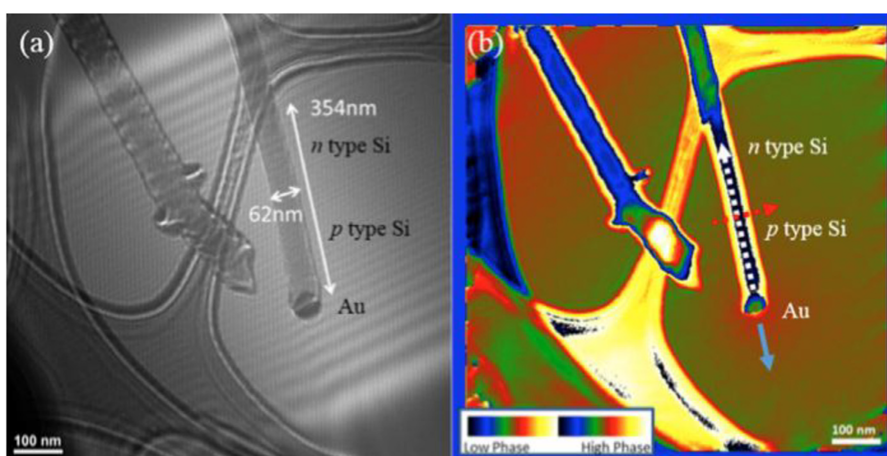

Fig. 9. (a) Off-axis electron hologram of a doped Si NW supported on a holey C film; (b) Reconstructed phase image visualized with pseudo-color. Reprinted from [85].

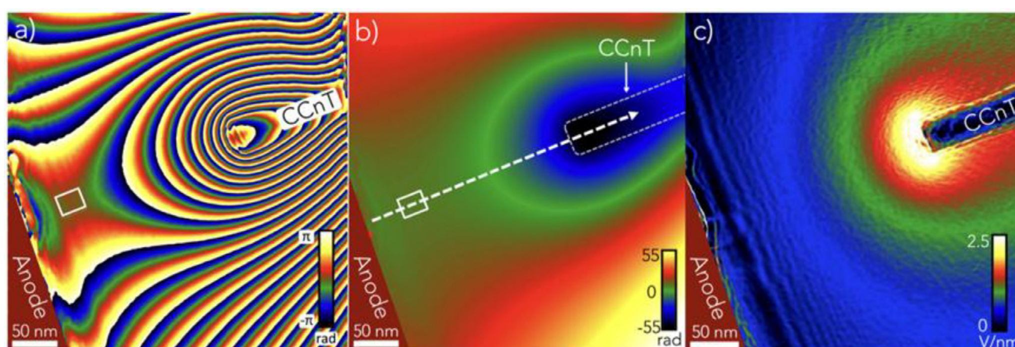

Fig. 10. (a) Experimental phase contours measured using off-axis electron holography from a field-emitting C nanocone at an applied voltage of 80 V. Similar colored lines correspond to phase shift of 2π. (b) Unwrapped version of (a). Color scale at bottom right. (c) Gradient of the phase, corresponding to the integrated electric field (Courtesy of Ludvig de Knoop).

nanotips, for which the onset of field emission occurred for an applied voltage of 80 V, and the local electric field was then estimated to be ~2.55 V/nm [102].

A model-independent method has been developed to enable the projected charge density distribution in a TEM specimen to be measured directly from the Laplacian of a recorded electron holographic phase image [105]. This approach has been applied to the measurement of the charge density in an electrically biased bundle of single-walled carbon nanotubes [105] and the amount of electron-beam-induced charge on an MgO nanoparticle [68]. When using this approach, contributions to the recorded phase from local variations in MIP and specimen thickness must be carefully considered, in order to avoid misinterpretation of the recovered charge density distribution [106]. Fig. 11 shows results obtained from an electrically biased Fe needle [104]. In this study, a voltage was applied between the needle and a counter-electrode that was placed coaxially with the needle at a distance of ~400 nm. Subtraction of the magnetic and MIP contributions to the recorded phase shift was achieved by evaluating the difference between aligned phase images recorded at two different bias voltages, as illustrated in Fig. 11(a)–(c). A cumulative charge profile along the needle measured from the resulting phase-difference image using the model-independent (Laplacian) approach revealed the presence of charge accumulation at the needle apex. The 3D electrostatic potential and electric field around the needle were inferred assuming cylindrical symmetry. Fig. 11(d) shows a central slice of the resulting 3D potential (colors) and electric field (white lines) around the needle.

4.6. Electrical biasing experiments

Off-axis electron holography has been used to study changes in the internal electrostatic potential distribution in semiconductor devices during *in situ* electrical biasing of TEM specimens. Such studies become more challenging for reduced specimen dimensions, in particular because of the need to fabricate and apply nanoscale electrical contacts to electron-transparent TEM specimens. The possible presence of series and parallel current leakage paths must be considered, and special attention must be paid to the specimen-contact geometry to ensure that reliable, quantitative results are obtained.

Early electrical biasing studies of chemically-thinned Si samples enabled the visualization of external electrostatic fringing fields close to the positions of *p-n* junctions [46]. Subsequently, studies of electrostatic potential profiles were performed as a function of electrical bias on Si *p*-

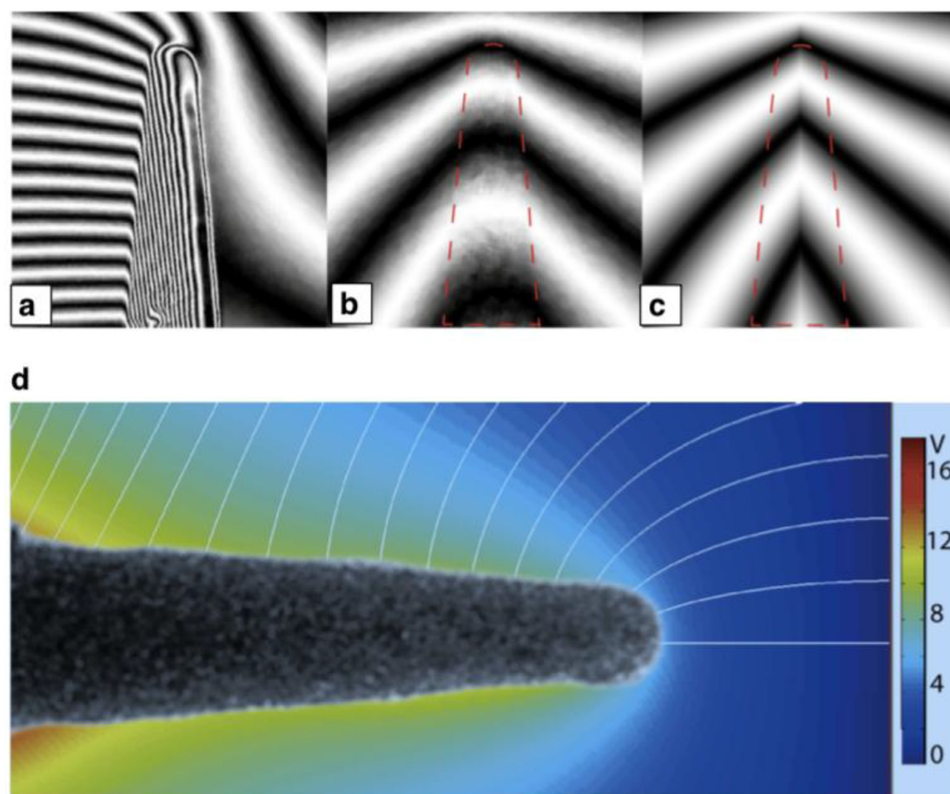

Fig. 11. (a)–(c) Equiphase contours recorded using off-axis electron holography from an electrically biased Fe needle. A voltage was applied between the needle and a counter-electrode that was placed coaxially with the needle with a lateral separation of ~400 nm. The images correspond to: (a) Original phase image recorded from the needle; (b) Difference between phase images acquired at two different bias voltages; (c) Best-fitting model-dependent simulation to the phase outside the needle shown in (b), based on a line charge model. (d) Central slice of the three-dimensional distribution of electrical potential (colors), and electric field (white lines), around the needle, inferred from the results shown in (a)–(c) on the assumption of cylindrical symmetry. Reprinted from [104].

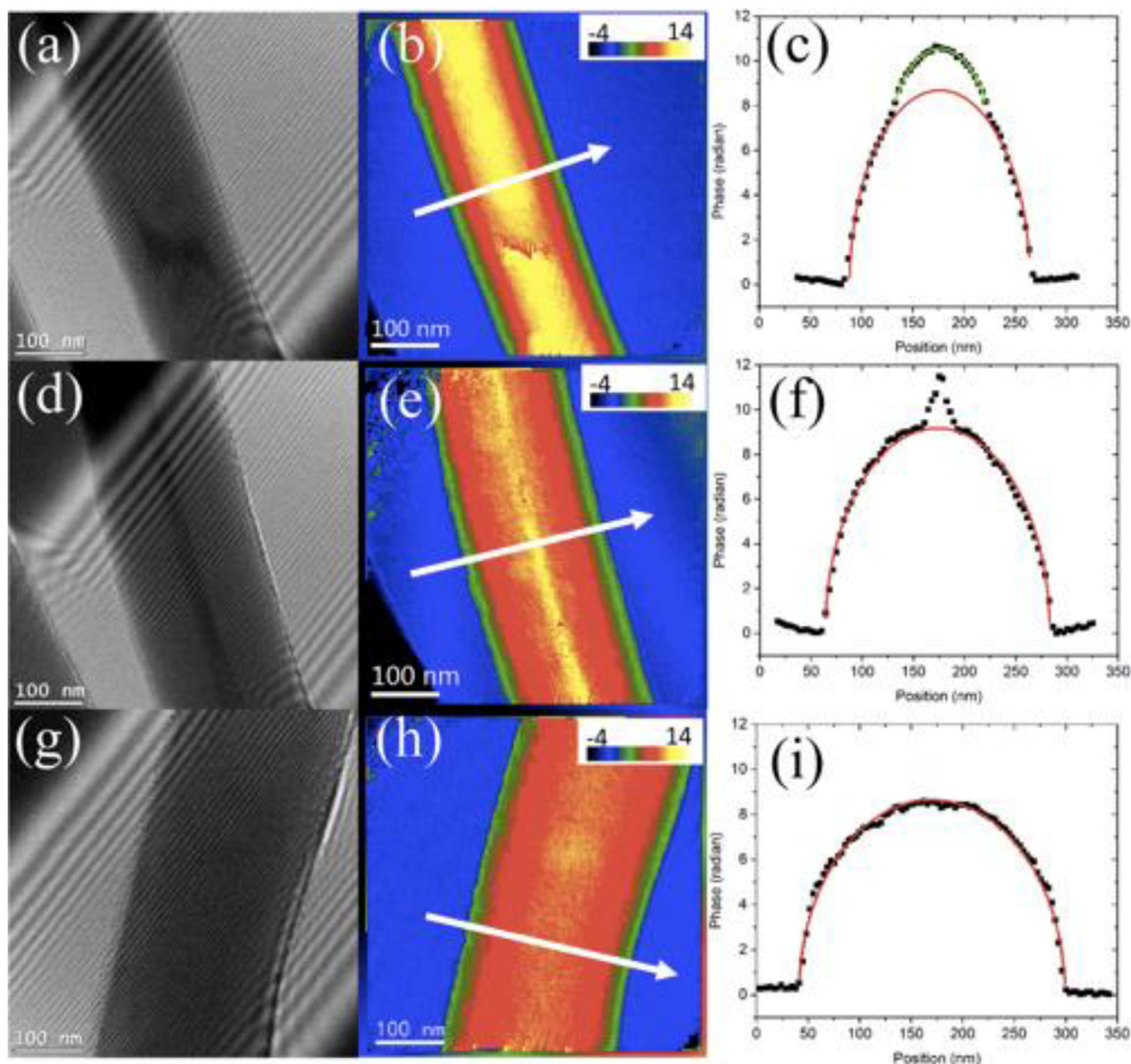

Fig. 12. Off-axis electron holography of Ge/Li_xGe core/shell nanowires during lithiation: (a, d and g) Off-axis electron holograms; (b, e and h) Corresponding reconstructed phase images, shown in pseudocolor. (Color scale shown at top right in units of radians); (c, f and i) Phase profiles extracted along the white arrows in b, e, and h, respectively. Reprinted from [110].

n junction devices that had been prepared for TEM examination using FIB milling [35, 38, 107]. A similar study of a reverse-biased GaAs *p-n* junction showed the expected built-in potential [54]. Changes in potential measured across a Si n^+-p junction as a function of forward and reverse bias were found to be in reasonable agreement with computer simulations [108]. *In situ* electrical biasing of GaN-based light-emitting diodes showed some junction contrast, but the measured change in potential of ~0.68 V was lower than the expected value of ~3.3 V, and did not change with applied bias, possibly because of the presence of a surface shunting resistance [109].

Off-axis electron holography has been used to map the charge density distribution during lithiation of Ge NWs subjected to *in situ* electrical biasing [110]. Fig. 12 shows the lithiation process leading progressively to expansion of the Li_xGe shell surrounding a shrinking Ge NW core. Electron holography was used to show that the surface region of the core had become negatively charged, while the inner surface of the shell had developed a counterbalancing positive charge. A Schottky contact and an axial depletion width in an electrically biased ZnO NW were recently studied using electron holography as a function of reverse bias [111]. Comparisons with simulations revealed an *n*-type doping level of $1 \times 10^{18}/cm^3$ and a negative sidewall charge of $2.5 \times 10^{12}/cm^2$.

Electron holography observations of solid-state Li-ion batteries, which are potential replacements for liquid-ion-based variants, have revealed changes in electrostatic potential distribution during charge-discharge cycling [112, 113]. In this study, external electrostatic fringing fields, surface damage from FIB sample preparation, and surface oxidation during exposure to air, all had to be taken into consideration [114]. Strategies to mitigate these effects are being evaluated [115, 116].

5. Challenges and opportunities

Reliable sample preparation and artifact-free phase imaging are major ongoing concerns for off-axis electron holography of nanoscale electrostatic potentials and charge density distributions, especially for

investigations of semiconductor devices with reduced feature sizes, which can be affected significantly by surface charging and the presence of native oxides. Other artifacts that complicate the quantification of electrostatic fields are associated with charging of TEM specimens due to the emission of secondary electrons during imaging, and the production of electron-hole pairs in the specimen and their possible trapping at interfaces, defects and surfaces. Methods to circumvent and/or account for these effects should be considered in future experiments, for example by using *in situ* electrical biasing specimen holders. Studies by ourselves (e.g., [59, 108]) and others (e.g., [87]) have demonstrated successful *in situ* electrical biasing of doped Si-based junctions and NWs, allowing the direct measurement of changes in depletion width and built-in voltage as a function of applied bias. Electrical biasing also allows the degree of dopant activation to be determined through comparisons with device simulations [86]. The use of sample biasing during electron holography observations introduces an additional degree of freedom that can be decisive for identifying and accounting for other artifacts, such as surface pinning and the presence of trapped charges [54], which may otherwise complicate reliable electron hologram interpretation and quantification. Sample biasing can also be useful for allowing surface and interface charging effects due to sample preparation and/or electron beam irradiation to be distinguished from the built-in potentials and sheet charge density distributions that are of primary interest. Moreover, the measurement of dopant profiles and trapped charge density distributions with nanometer-scale spatial resolution will continue to benefit from the ability to modify depletion regions during observation using *in situ* forward/reverse biasing. The knowledge provided by such electron holography studies may be pivotal for the development of next-generation electronic and optoelectronic devices.

Semiconductor NWs continue to attract attention from the materials science and physics communities, especially because of the novel photonic, electronic and thermal properties that are associated with quantum confinement effects arising from their 1D geometry [117]. Different methods of NW synthesis continue to be explored, and techniques for the characterization of structure-property relationships are of interest and relevance. The realization of practical electronic devices based on semiconductor NWs is challenging, since precise control over dopant incorporation and activation is required. Doping has been realized during NW growth, for example by using gas-phase deposition [118], and ion implantation [119]. However, the measurement of activated dopant concentrations in NW geometries is far from straightforward, especially as dopant diffusion may occur during thermal annealing [120]. As mentioned above, off-axis electron holography can be used to measure electrostatic potential profiles caused by activated dopants, which can then be compared with device measurements and/or simulations [85, 86].

Full 3D tomographic mapping of electrostatic potentials and charge density distributions requires the acquisition of multiple electron holograms over a wide range of sample tilt angles (typically ± 70° in 2° steps), as well as reference electron holograms, albeit at less frequent intervals [53]. The influence of progressive changes in projected sample thickness becomes greater at larger sample tilt angles [121], and electron holograms that were recorded with the sample in strongly diffracting conditions may need to be discarded before performing tomographic reconstruction. Despite these challenges, successful 3D mapping of different semiconductor combinations has been achieved, and further holography- tomography studies can be anticipated in the future.

Many of the above considerations also apply to results obtained using other modes of electron holography, such as phase-shifting electron holography [122] and in-line electron holography [123, 124]. These techniques offer some strategic advantages over off-axis electron holography for investigating electrostatic potentials in certain types of specimens. However, studies of electrostatic potentials reported in the literature using these techniques are still limited in number. The technique of phase-shifting electron holography involves recording a series of off-axis electron holograms with different incident beam tilt angles, in order to reconstruct a phase image with higher spatial resolution and higher phase measurement sensitivity [122]. Electrostatic potential variations in a GaAs *p-n-p* test sample with high ($3.0 \times 10^{18}/cm^2$) and low ($1.3 \times 10^{16}/cm^2$) dopant concentrations were mapped using this approach [125], while later studies of a biased GaAs *p-n* tunnel junction showed a built-in potential of 1.55 ± 0.02 V, and changes in depletion width as a function of applied voltage have also been measured [126]. The technique of in-line electron holography involves recording a defocus series of images, from which the complex electron wavefunction can be reconstructed [124]. It is reported to be as quantitative as off-axis electron holography, and to be applicable to samples for which the off-axis technique cannot be applied due to the lack of a reference wave [127]. It can be challenging to recover the lowest spatial frequencies in the phase using in-line electron holography. Nevertheless, the technique has recently been used to examine the spatial confinement of a 2DEG for different orientations of $LaAlO_3$/$SrTiO_3$ interfaces [128].

6. Concluding remarks

This paper has focused on the quantitative characterization of electrostatic potentials and charge density distributions with nanoscale spatial resolution using the technique of off-axis electron holography. Examples encompassing a wide range of materials have been presented, and many more applications can be anticipated. In the future, attention should be devoted to improvements in sample preparation to reduce roughness, oxidation and contamination, to the development of improved specimen geometries for complex *in situ* experiments with both fixed and movable electrical contacts, and to the development of approaches for reducing dynamical contributions to recorded phase images. Systems of interest include electrical double layers at solid-liquid interfaces imaged during electrochemical experiments. In addition, possibilities for ultrafast and dynamic experiments should be explored, for example using electron microscopes that are equipped with pulsed coherent electron sources. There are many good reasons to be optimistic about the future of off-axis electron holography, cementing the legacy of Hannes Lichte in this research field [129].

Acknowledgments

M.R.M. and D.J.S are pleased to acknowledge Suk Chung, David Cullen, Zhaofeng Gan, Myung-Geun Han, Jing Li, Luying Li, and Lin Zhou for their contributions to some of the off-axis electron holography studies described here. R.D.-B. thanks Vadim Migunov, Fengshan Zheng, Giulio Pozzi, Amir H. Tavabi, Lionel C. Gontard, Marco Beleggia, Andrew London, Michael Farle, Tom F. Kelly, David Cooper, Alison Twitchett-Harrison and Paul A. Midgley for past and ongoing collaborations. M.R.M. and D.J.S. are grateful for funding from DOE Grant DE-FG02-04ER46168. R.D.-B. is grateful for funding from the European Union through the Marie Curie Initial Training Network SIMDALEE2 (Marie Curie Initial Training Network (ITN) grant no. 606998 under FP7-PEOPLE-2013-ITN), from the Deutsche Forschungsgemeinschaft within the framework of the SFB 917 project “Nanoswitches", from the Deutsche Forschungsgemeinschaft for a Deutsch-Israelische Projektkooperation (DIP) Grant and from the European Union's Horizon 2020 Research and Innovation Programme Q-SORT (grant no. 766970 under H2020-FETOPEN-2016-2017). We acknowledge the use of facilities in the John M. Cowley Center for High Resolution Electron Microscopy in Arizona State University and the Ernst Ruska-Centre for Microscopy and Spectroscopy with Electrons in Forschungszentrum Jülich. Finally, we express our deep admiration and sincere appreciation to Hannes Lichte for his inspiration, encouragement, and invaluable contributions to the field of electron holography across the years.

References

[1] D. Gabor, Microscopy by reconstructed wavefronts, Proc. Roy. Soc. A 197 (1949) 454.
[2] A. Tonomura, T. Matsuda, J. Endo, H. Todokoro, T. Komoda, Development of field-emission electron microscope, J. Electron. Microsc. 28 (1979) 1–11.
[3] J.M. Cowley, Twenty forms of electron holography, Ultramicroscopy 41 (1992) 335–348.
[4] A. Orchowski, W.D. Rau, H. Lichte, Electron holography surmounts resolution limit of electron microscopy, Phys. Rev. Lett. 74 (1995) 399–402.
[5] D. Geiger, H. Lichte, M. Linck, M. Lehmann, Electron holography with a C(s)-corrected transmission electron microscope, Microsc. Microanal. 14 (2008) 68–81.
[6] M.R. McCartney, D.J. Smith, Electron holography: Phase imaging with nanometer resolution, Annu. Rev. Mater. Res. 37 (2007) 729.
[7] H. Lichte, Electron image plane off-axis holography of atomic structures, Adv. Opt. Electron Microsc. 12 (1991) 25–91.
[8] A. Tonomura, Electron-holographic interference microscopy, Adv. Phys. 41 (1992) 59–103.
[9] P.A. Midgley, An introduction to off-axis electron holography, Micron 32 (2001) 167–184.
[10] G. Matteucci, G.F. Missiroli, G. Pozzi, Electron holography of long-range electrostatic fields, Adv. Imaging Electron Phys. 122 (2002) 173–249.
[11] H. Lichte, P. Formanek, A. Lenk, M. Linck, C. Matzeck, M. Lehmann, P. Simon, Electron holography: Applications to materials questions, Ann. Rev. Mater. Res. 37 (2007) 539–588.
[12] P.A. Midgley, R.E. Dunin-Borkowski, Electron tomography and holography in materials science, Nat. Mater. 8 (2009) 271–280.
[13] G. Pozzi, M. Beleggia, T. Kasama, R.E. Dunin-Borkowski, Interferometric methods for mapping static electric and magnetic fields, Comptes Rendus. Phys. 15 (2013) 126–139.
[14] R.E. Dunin-Borkowski, A. Kovács, T. Kasama, M.R. McCartney, D.J. Smith, Electron holography, in: P.W. Hawkes, J.C.H. Spence (Eds.), Handbook of Microscopy, Springer, 2019in press.
[15] G. Möllenstedt, H. Düker, Fresnelscher interferenzversuch mit einem biprisma fur elektronenwellen, Naturwiss 42 (1955) 41.
[16] L. Reimer, Transmission Electron Microscopy, Springer, Berlin, 1991.
[17] D. Wolf, A. Lubk, F. Roder, H. Lichte, Electron holographic tomography, Curr. Opinion Solid State Mater. Sci. 17 (2013) 126–134.
[18] M. Gajdardziska-Josifovska, A Carim, Applications of electron holography, in: E. Völkl, L.F. Allard, D.C. Joy (Eds.), Introduction to Electron Holography, Kluwer, New York, 1999, pp. 241–266 Chapter 12.
[19] J. Li, M.R. McCartney, D.J. Smith, Semiconductor dopant profiling by off-axis electron holography, Ultramicroscopy 94 (2003) 149–161.
[20] S. Chung, D.J. Smith, M.R. McCartney, Determination of the inelastic mean-free-path and mean inner potential for AlAs and GaAs using off-axis electron holography and convergent beam electron diffraction, Microsc. Microanal. 13 (2007) 329–335.
[21] M.R. McCartney, M. Gajdardziska-Josikovska, Absolute measurement of normalized thickness, t/λ_i, from off-axis electron holography, Ultramicroscopy 53 (1993) 283–289.
[22] H. Lichte, M. Lehmann, Electron holography—basics and applications, Rep. Prog. Phys. 71 (2008) 016102.
[23] H. Lichte, Electron holography approaching atomic resolution, Ultramicroscopy 20 (1986) 293–304.
[24] W.J. de Ruijter, J.K. Weiss, Detection limits in quantitative off-axis electron holography, Ultramicroscopy 50 (1993) 269–283.
[25] D. Cooper, R. Truche, P. Rivallin, J.-M. Hartmann, F. Laugier, F. Bertin A. Chabli, Medium resolution off-axis electron holography with millivolt sensitivity, Appl. Phys. Lett. 91 (2007) 143501.
[26] D.J. Smith, M.R. McCartney, Practical electron holography, in: E Völkl, LF Allard, DC. Joy (Eds.), Introduction to Electron Holography, Kluwer, New York, 1999, pp. 87–106.
[27] M.-G. Han, J. Li, Q. Xie, P. Fejes, J. Connor, B. Taylor, M.R. McCartney, Sample preparation for precise and quantitative electron holographic analysis of semiconductor devices, Microsc. Microanal. 12 (2006) 295–301.
[28] Z. Gan, M. DiNezza, Y.-H. Zhang, D.J. Smith, M.R. McCartney, Determination of mean inner potential and inelastic mean free path of ZnTe using off-axis electron holography and dynamical effects affecting phase determination, Microsc. Microanal. 21 (2015) 1406–1412.
[29] P. Formanek, E. Bugiel, On specimen tilt for electron holography of semiconductor devices, Ultramicroscopy 106 (2006) 292–300.
[30] M.R. McCartney, Characterization of charging in semiconductor device materials by electron holography, J. Electron Microsc. 54 (2005) 239–242.
[31] J. Bravman, R. Sinclair, The preparation of cross-section specimens for transmission electron microscopy, J. Electron Microsc. Tech. 1 (1984) 53–61.
[32] W.D. Rau, P. Schwander, F.H. Baumann, W. Hoppner, A. Ourmazd, Two-dimensional mapping of the electrostatic potential in transistors by electron holography, Phys. Rev. Lett. 82 (1999) 2614–2617.
[33] L.A. Giannuzzi, F.A. Stevie, Introduction to Focused Ion Beams, Springer, New York, 2005.
[34] R.E. Dunin-Borkowski, S.B. Newcomb, T. Kasama, M.R. McCartney, M. Weyland, P.A. Midgley, Conventional and back-side focused ion beam milling for off-axis electron holography of electrostatic potentials in transistors, Ultramicroscopy 103 (2005) 67–81.
[35] A.C. Twitchett, R.E. Dunin-Borkowski, R.J. Hallifax, R.F. Broom, P.A. Midgley, Off-axis electron holography of unbiased and reverse-biased focused ion beam milled Si *p-n* junctions, Microsc. Microanal. 11 (2005) 66–78.
[36] Z.G. Wang, T. Kato, N. Shibata, T. Hirayama, N. Kato, K. Sasaki, H. Saka, Characterizing an implanted Si/Si *p-n* junction with lower doping level by combined electron holography and focused-ion-beam milling, Appl. Phys. Lett. 81 (2002) 4780490.
[37] Z.G. Wang, T. Kato, T. Hirayama, K. Sasaki, H. Saka, N. Kato, Focused-ion-beam preparation of wedge-shaped cross sections and its application to observing *p-n* junctions by electron holography, J. Vac. Sci. Technol. B 21 (2003) 2155–2158.
[38] A.C. Twitchett, R.E. Dunin-Borkowski, P.A. Midgley, Quantitative electron holography of biased semiconductor devices, Phys. Rev. Lett. 88 (2002) 238302.
[39] D. Cooper, A.C. Twitchett, P.K. Somodi, P.A. Midgley, R.E. Dunin-Borkowski, I. Farrer, D.A. Ritchie, Improvement in electron holographic phase images of focused-ion-beam-milled GaAs and Si *p-n* junctions by *in situ* annealing, Appl. Phys. Lett. 88 (2006) 063510.
[40] N. Ikarashi, T. Ikezawa, K. Uejima, T. Fukai, M. Miyamura, A. Toda, M. Hane, Electron holography analysis of a shallow junction for planar-bulk metal-oxide-semiconductor field-effect transistors approaching the scaling limit, J. Appl. Phys. 103 (2008) 114514.
[41] P. Formanek, E. Bugiel, Specimen preparation for electron holography of semiconductor devices, Ultramicroscopy 106 (2006) 365–375.
[42] D. Cooper, C. Ailliot, J.P. Barnes, J.-M. Hartmann, P. Salles, G. Benassayag, R.E. Dunin-Borkowski, Dopant profiling of focused ion beam milled semiconductors using off-axis electron holography: Reducing artifacts, extending detection limits and reducing the effects of gallium implantation, Ultramicroscopy 110 (2010) 383–389.
[43] M.A. Gribelyuk, M.R. McCartney, J. Li, C.S. Murthy, P. Ronsheim, B. Doris, J.S. McMurray, S. Hegde, D.J. Smith, Mapping of electrostatic potential in deep submicron CMOS devices by electron holography, Phys. Rev. Lett. 89 (2002) 025502.
[44] A. Diebold, M.R. Kump, J.J. Kopanski, D.G. Seiler, Characterization of two-dimensional dopant profiles: Status and review, J. Vac. Sci. Technol. B 14 (1996) 196–201.
[45] G. Matteucci, G.F. Missiroli, G. Pozzi, P.G. Merli, I. Vecchi, Interference electron-microscopy in thin-film investigations, Thin Solid Films 62 (1979) 5–17.
[46] S. Frabboni, G. Matteucci, G. Pozzi, M. Vanzi, Electron holographic observations of the electrostatic field associated with thin reverse-biased *p*-n junctions, Phys. Rev. Lett. 55 (1985) 2196–2199.
[47] M.R. McCartney, D.J. Smith, R. Hull, J.C. Bean, E. Völkl, B.G. Frost, Direct observation of potential distribution across Si/Si *p-n* junctions using off-axis electron holography, Appl. Phys. Lett. 65 (1994) 2603–2605.
[48] M.R. McCartney, M.A. Gribelyuk, J. Li, P. Ronsheim, J.S. McMurray, D.J. Smith, Quantitative analysis of one-dimensional dopant profile by electron holography, Appl. Phys. Lett. 80 (2002) 3213–3215.
[49] A. Lenk, H. Lichte, U. Muehle, 2D-mapping of dopant distribution in deep submicron CMOS devices by electron holography using adapted FIB-preparation, J. Electron Microsc. 54 (2005) 351–359.
[50] M.-G. Han, P. Fejes, Q. Xie, S. Bagchi, B. Taylor, J. Conner, M.R. McCartney, Quantitative analysis of 2-D electrostatic potential distributions in 90-nm Si pMOSFETs using off-axis electron holography, IEEE Trans. Electron Devices 54 (2007) 3336–3341.
[51] N. Ikarashi, M. Oshida, M. Miyamura, M. Saitoh, A. Mineji, S. Shishiguchi, Electron holography characterization of ultra shallow junctions in 30-nm-gate-length metal-oxide-semiconductor field-effect transistors, Jap. J. Appl. Phys. 47 (2008) 2365–2368.
[52] N. Ikarashi, N. Takeda, K. Yako, M. Hane, *In situ* electron holography of surface potential response to gate voltage application in a sub-30-nm gate-length metal-oxide-semiconductor field-effect transistor, Appl. Phys. Lett. 100 (2012) 143508.
[53] A.C. Twitchett-Harrison, J.T.V. Yates, S.B. Newcomb, R.E. Dunin-Borkowski, P.A. Midgley, High-resolution three-dimensional mapping of semiconductor dopant potentials, Nano Letts 7 (2007) 2020–2023.
[54] D. Cooper, R. Truche, A.C. Twitchett-Harrison, R.E. Dunin-Borkowski, P.A. Midgley, Quantitative off-axis electron holography of GaAs *p-n* junctions prepared by focused ion beam milling, J. Microsc. 233 (2009) 102–113.
[55] M.A. Gribelyuk, A.G. Domenicucc, P.A. Ronsheim, J.S. McMurray, O. Gluschenkov, Application of electron holography to analysis of submicron structures, J. Vac. Sci. Tech. B 26 (2008) 408–414.
[56] N. Ikarashi, A. Toda, K. Uejima, K. Yako, T. Yamamoto, M. Hane, H. Sato, Electron holography for analysis of deep submicron devices: Present status and challenges, J. Vac. Sci. Technol B 28 (2010) C1D5–C1D10.
[57] D. Cooper, F. de la Pena, A. Beche, J.-L Rouviere, G. Servanton, R. Pantel, P. Morin, Field mapping with nanometer-scale resolution of the next generation of electronic devices, Nano Lett. 11 (2011) 4585–4590.
[58] M.A. Gribelyuk, V. Ontalus, F.H.J. Baumann, Z. Zhu, J.R. Holt, Electron holography of devices with epitaxial layers, J. Appl. Phys. 116 (2014) 174501.
[59] S. Yazdi, T. Kasama, M. Beleggia, M.S. Yekta, D.W. McComb, A.C. Twitchett-Harrison, R.E. Dunin-Borkowski, Towards quantitative electrostatic potential mapping of working semiconductor devices using off-axis electron holography, Ultramicroscopy 152 (2015) 10–20.
[60] D. Cooper, Off-axis electron holography for the measurement of active dopants in silicon semiconductor devices, J. Phys. D 49 (2016) 1–23.
[61] L. Li, S. Ketharananthan, J. Drucker, M.R. McCartney, Study of hole accumulation in individual germanium quantum dots in *p*-type silicon by off-axis electron holography, Appl. Phys. Lett. 94 (2009) 232108.
[62] L. Zhou, D.J. Smith, M.R. McCartney, T. Xu, T.D. Moustakas, Measurement of electric field across individual wurtzite GaN quantum dots using electron

holography, Appl. Phys. Lett. 99 (2011) 101905.
[63] J. Cai, F.A. Ponce, Determination by electron holography of the electronic charge distribution at threading dislocations in epitaxial GaN, *phys. stat. sol.* (a) 192 (2002) 407–411.
[64] D. Cherns, C.G. Jiao, Electron holography studies of the charge on dislocations in GaN, Phys. Rev. Lett. 87 (2001) 205504.
[65] E. Müller, D. Gerthsen, P. Brückner, F. Scholz, T. Gruber, A. Waag, Probing the electrostatic potential of charged dislocations in *n*-GaN and *n*-ZnO epilayers by transmission electron holography, Phys. Rev. B 73 (2006) 245316.
[66] E. Müller, D. Gerthsen, P. Brückner, F. Scholz, C. Kirchner, A. Waag, Electrical activity of dislocations in epitaxial ZnO- and GaN-layers analyzed by holography in a transmission electron microscope, Maters. Sci. Semiconduct. Proc. 9 (2006) 127–131.
[67] S. Chung, R.A. Berechman, M.R. McCartney, M. Skowronski, Electronic structure analysis of threading screw dislocations in 4H-SiC using electron holography, J. Appl. Phys. 109 (2011) 043906.
[68] C. Gatel, A. Lubk, G. Pozzi, E. Snoeck, M. Hÿtch, Counting elementary particles by electron holography, Phys. Rev. Lett. 111 (2013) 025501.
[69] L. Li, X. Hu, Y. Gao, Electron holographic study of semiconductor light-emitting diodes, Small 14 (2018) 14.
[70] D. Cherns, H. Mokhtari, C.G. Jiao, R. Averback, H. Riechert, Profiling band structure in GaN devices by electron holography, J. Cryst. Growth 230 (2001) 410–414.
[71] J. Cai, F.A. Ponce, Study of charge distribution across interfaces in GaN/InGaN/GaN single quantum wells using electron holography, J. Appl. Phys. 91 (2002) 9856–9862.
[72] J. Cai, F.A. Ponce, S. Tanaka, H. Omiya, Y. Nakagawa, Mapping the internal potential across GaN/AlGaN heterostructures by electron holography, *phys. stat. sol.* (a) 188 (2001) 833–837.
[73] Z.H. Wu, M. Stevens, F.A. Ponce, W. Lee, J.H. Ryou, D. Yoo, R.D. Dupuis, Mapping the electrostatic potential across AlGaN/AlN/GaN heterostructures using electron holography, Appl. Phys. Lett. 90 (2007) 032101.
[74] M.R. McCartney, F.A. Ponce, J. Cai, D.P. Bour, Mapping electrostatic potential across an AlGaN/InGaN/GaN diode by electron holography, Appl. Phys.Lett. 76 (2000) 3055–3057.
[75] J.S. Barnard, M.J. Kappers, E.J. Thrush, C.J. Humphreys, Electrostatic fields in InGaN/GaN single quantum wells and their variation with indium content, using off-axis electron holography and energy filtered TEM, Inst. Phys. Conf. Ser. 180 (2003) 281–284.
[76] M. Stevens, A. Bell, M.R. McCartney, F.A. Ponce, H. Marui, S. Tanaka, Effect of layer thickness on the electrostatic potential in InGaN quantum wells, Appl. Phys. Lett. 85 (2004) 4651–4653.
[77] C. McAleese, P.M.F.J. Costa, D.M. Graham, H. Xiu, J.S. Barnard, M.J. Kappers, P. Dawson, M.J. Godfrey, C.J. Hunphreys, Electric fields in AlGaN/GaN quantum well structures, Phys. Stat. sol. (b) 7 (2006) 1551–1559.
[78] Q. Wei, Z. Wu, K. Sun, F.A. Ponce, J. Hertkorn, F. Scholz, Evidence of two-dimensional hole gas in p-type AlGaN/AlN/GaN heterostructures, Appl. Phys. Expr. 2 (2009) 121001.
[79] L. Zhou, D.A. Cullen, D.J. Smith, M.R. McCartney, A. Mouti, M. Gonsherek, E. Feltin, J.F. Carlin, N. Grandjean, Polarization field mapping of $Al_{0.85}$ $In_{0.15}N$/AlN/GaN heterostructure, Appl. Phys. Lett. 94 (2009) 121909.
[80] L. Zhou, E. Dimakis, R. Hathwar, T. Aoki, D.J. Smith, T.D. Moustakas, S.M. Goodnick, M.R. McCartney, Measurement and effects of polarization fields on one-monolayer-thick InN/GaN multiple quantum wells, Phys. Rev. B 88 (2013) 125310.
[81] M.I.den Hertog, H. Schmid, D. Cooper, J.-L. Rouviere, M.T. Bjork, H. Riel, P. Rivallin, S. Karg, W. Riess, Mapping active dopants in single silicon nanowires using off-axis electron holography, Nano Letts 9 (2009) 3837–3843.
[82] J. Chung, L. Rabenberg, Mapping of electrostatic potentials within core-shell nanowires by electron holography, Appl. Phys. Lett. 88 (2006) 013106.
[83] L. Li, D.J. Smith, E. Dailey, P. Madras, J. Drucker, M.R. McCartney, Observation of hole accumulation in Ge/Si core/shell nanowires using off-axis electron holography, Nano Letts 11 (2011) 493–497.
[84] A. Darbandi, J.C. McNeil, A. Aktari-Zavareh, S.P. Watkins, K.L. Kavanagh, Direct measurement of the electrical abruptness of a nanowire p-n junction, Nano Letts 16 (2016) 3982–3988.
[85] Z. Gan, D.E. Perea, J. Yoo, S.T. Picraux, D.J. Smith, M.R. McCartney, Mapping electrostatic profiles across axial *p-n* junctions in Si nanowires using off-axis electron holography, Appl. Phys. Lett. 103 (2013) 153108.
[86] Z. Gan, D. Perea, J. Yoo, Y. He, R. Colby, J.E. Barker, M. Gu, S.X. Mao, C. Wang, S.T. Picraux, D.J. Smith, M.R. McCartney, Characterization of electrical properties in axial Si-Ge nanowire heterojunctions using off-axis electron holography and atom-probe tomography, J. Appl. Phys. 120 (2016) 104301.
[87] K. He, J.-H. Cho, Y. Jung, S.T. Picraux, J. Cumings, Silicon nanowires: Electron holography studies of doped p-n junctions and biased Schottky barriers, Nanotechnology 24 (2013) 115703.
[88] S. Yazdi, A. Berg, M.T. Borgström, T. Kasama, M. Belaggia, L. Samuelson, J.B. Wagner, Doping GaP core-shell nanowire *pn*-junctions: A study using off-axis electron holography, Small 11 (2015) 2687–2695.
[89] J.P. Boulanger, A.C.E. Chia, B. Wood, S. Yazdi, T. Kasama, M. Aagesen, R.R. LaPierre, Characterization of a Ga-assisted GaAs nanowire array solar cell on Si substrate, IEEE J. Photovoltaics 6 (2016) 661–667.
[90] L. Li, Z. Gan, M.R. McCartney, H. Liang, H. Yu, W.-J. Yin, Y. Yan, Y. Gao, J. Wang, D.J. Smith, Determination of polarization fields across polytype interfaces in InAs nanopillars, Adv. Mater. 26 (2014) 1052–1057.
[91] L. Li, L. Jin, J. Wang, D.J. Smith, W.-J. Yin, Y. Yan, H. Song, W.C.H. Choy, M.R. McCartney, Polarization-induced charge distribution at homogeneous zinc-blende/ wurtzite heterostructural junctions in ZnSe nanobelts, Adv. Maters. 24 (2012) 1328–1332.
[92] D. Wolf, H. Lichte, G. Pozzi, P. Prete, N. Lovergine, Electron holographic tomography for mapping the three-dimensional distribution of electrostatic potential in III-V semiconductor nanowires, Appl. Phys. Lett. 98 (2011) 264103.
[93] A. Lubk, D. Wolf, P. Preto, N. Lovergine, T. Niermann, S. Sturm, H. Lichte, Nanometer-scale tomographic reconstruction of three-dimensional electrostatic potentials in GaAs/AlGaAs core-shell nanowires, Phys. Rev. B 90 (2014) 125404.
[94] D. Wolf, A. Lubk, P. Prete, N. Lovergine, H. Lichte, 3D mapping of nanoscale electric potentials in semiconductor structures using electron holographic tomography, J. Phys. D 49 (2016) 364004.
[95] D. Wolf, R. Hubner, T. Niermann, S. Sturm, P. Prete, N. Lovergine, B. Buchner, A. Lubk, Three-dimensional composition and electric potential mapping of III-V core-multishell nanowires by correlative STEM and holographic tomography, Nano Letts 18 (2018) 4777–4784.
[96] G. Matteucci, G.F. Missiroli, M. Muccini, G. Pozzi, Electron holography in the study of the electrostatic fields—the case of charged microtips, Ultramicroscopy 45 (1992) 77–83.
[97] G. Matteucci, G.F. Missiroli, G. Pozzi, Electron interferometry and holography of electrostatic fields—fundamental and applicative aspects, Phys. B 151 (1988) 223–229.
[98] T. Kawasaki, G.F. Missiroli, G. Pozzi, A. Tonomura, Multiple-beam experiments with a holographic electron microscope, Optik 92 (1993) 168–174.
[99] J. Cumings, A. Zettl, M.R. McCartney, J.C.H. Spence, Electron holography of field-emitting carbon nanotubes, Phys. Rev. Lett. 88 (2002) 056804.
[100] J.J. Kim, D. Shindo, Y. Murakami, W. Xia, L.J. Chou, Y.L. Chueh, Direct observation of field emission in a single $TaSi_2$ nanowire, Nano Lett. 7 (2007) 2243–2247.
[101] F. Houdellier, A. Masseboeuf, M. Monthioux, M. Hÿtch, New carbon cone nanotip for use in a highly coherent cold field emission electron microscope, Carbon 50 (2012) 2037–2044.
[102] L. de Knoop, F. Houdellier, C. Gatel, A. Masseboeuf, M. Monthioux, M. Hÿtch, Determining the work function of a carbon-cone cold-field emitter by *in situ* electron holography, Micron 63 (2014) 2–8.
[103] M. Beleggia, T. Kasama, D.J. Larson, T.F. Kelly, R.E. Dunin-Borkowski, G. Pozzi, Towards quantitative off-axis electron holographic mapping of the electric field around the tip of a sharp biased metallic needle, J. Appl. Phys. 116 (2014) 024305.
[104] V. Migunov, A. London, M. Farle, R.E. Dunin-Borkowski, Model-independent measurement of the charge density distribution along an Fe atom probe needle using off-axis electron holography without mean inner potential effects, J. Appl. Phys. 117 (2015) 134301.
[105] M. Beleggia, T. Kasama, R.E. Dunin-Borkowski, S. Hofmann, G. Pozzi, Direct measurement of the charge distribution along a biased carbon nanotube bundle using electron holography, Appl. Phys. Lett. 98 (2011) 243101.
[106] M. Beleggia, L.C. Gontard, R.E. Dunin-Borkowski, Local charge measurement using off-axis electron holography, J. Phys. D: Appl. Phys. 49 (2016) 294003.
[107] A.C. Twitchett, R.-E. Dunin-Borkowski, R.J. Hallifax, R.F. Broom, P.A. Midgley, Off-axis electron holography of electrostatic potentials in unbiased and reverse biased focused ion beam milled semiconductor devices, J. Microsc. 214 (2004) 287–296.
[108] M.-G. Han, D.J. Smith, M.R. McCartney, *In situ* electron holographic analysis of biased Si n^+-p junctions, Appl. Phys. Lett. 92 (2008) 143502.
[109] L.Z.-Y. Liu, C. McAleese, D.V. Sridhara Rao, M.J. Kappers, C.J. Humphreys, Electron holography of an in-situ biased GaN LED, *phys. stat. sol.* (c) 9 (2012) 704–707.
[110] Z. Gan, M. Gu, J.S. Tang, C.Y. Wang, Y. He, K.L. Wang, C.M. Wang, D.J. Smith, M.R. McCartney, Direct mapping of charge distribution during lithiation of Ge nanowires using off-axis electron holography, Nano Lett 16 (2016) 3748–3753.
[111] M. den Hertog, F. Donatini, R. McLeod, E. Monroy, C. Sartel, V. Sailet, J. Pernot, *In situ* biasing and off-axis electron holography of a ZnO nanowire, Nanotechnology 29 (2018) 025710.
[112] K. Yamamoto, Y. Iriyama, T. Asaka, T. Hirayama, H. Fujita, C.A.J. Fisher, K. Nonaka, Y. Sugita, Z. Ogumi, Dynamic visualization of the electric potential in an all-solid-state rechargeable lithium battery, Angew. Chem. Int. Ed. 49 (2010) 4414–4417.
[113] K. Yamamoto, Y. Iriyama, T. Asaka, T. Hirayama, H. Fujita, K. Nonaka, K. Miyahara, Y. Sugita, Z. Ogumi, Direct observation of lithium-ion movement around an *in-situ*-formed-negative-electrode/solid-state-electrolyte interface during initial charge-discharge reaction, Electrochem. Commun. 20 (2012) 113–116.
[114] T. Hirayama, Y. Aizawa, K. Yamamoto, T. Sato, H. Murata, R. Yoshida, C.A.J. Fisher, T. Kato, T. Iriyama, Advanced electron holography techniques for *in situ* observation of solid-state lithium ion conductors, Ultramicroscopy 173 (2017) 64–70.
[115] Y. Nomura, K. Yamamoto, T. Hirayama, K. Saitoh, Electric shielding films for biased TEM samples and their application to *in situ* electron holography, Microscopy 67 (2018) 178–186.
[116] Y. Aizawa, K. Yamamoto, T. Sato, H. Murata, R. Yoshida, C.A.J. Fisher, T. Kato, Y. Iriyama, T. Hirayama, *In situ* electron holography of electric potentials inside a solid-state electrolyte: effect of electric-field leakage, Ultramicroscopy 178 (2017) 20–26.
[117] J.K. Hyun, S. Zhang, L.J. Lauhon, Nanowire heterostructures, Annu. Rev. Mater. Res. 43 (2013) 451–479.
[118] P. Agarwal, M.N. Vijayaraghavan, F. Neuilly, E. Hijzen, G.A.M. Hurkx, Breakdown

enhancement in silicon nanowire *p-n* junctions, Nano Letts. 7 (2007) 896–899.
[119] S. Hoffman, S. Bauer, C. Ronning, T. Stelzner, J. Michler, C. Ballif, V. Sivakov, S.H. Christiansen, Axial *p-n* junctions realized in silicon nanowires by ion implantation, Nano Letts. 9 (2009) 1341–1346.
[120] E. Koren, E. Berkovitch, Y. Rosenwaks, Measurement of active dopant distribution and diffusion in individual silicon nanowires, Nano Letts 10 (2010) 1163–1167.
[121] A.C. Twitchett-Harrison, J.T.V. Yates, R.E. Dunin-Borkowski, Quantitative electron holographic tomography for the 3D characterisation of semiconductor device structures, Ultramicroscopy 108 (2008) 1401–1407.
[122] K. Yamamoto, I Kawajiri, T. Tanji, M. Hibino, T. Hirayama, High precision phase-shifting electron holography, J. Electron Microsc. 49 (2000) 31–39.
[123] A.C. Twitchett, R.E. Dunin-Borkowski, P.A. Midgley, Comparison of off-axis and in-line electron holography as quantitative dopant-profiling techniques, Philos. Mag. 86 (2006) 5805–5823.
[124] C.T. Koch, A. Lubk, Off-axis and online electron holography: A quantitative comparison, Ultramicroscopy 110 (2010) 460–471.
[125] H. Sasaki, K. Yamamoto, T. Hirayama, S. Ootomo, T. Matsuda, F. Iwase, R. Nakasaki, H. Ishii, Mapping of dopant concentration in a GaAs semiconductor by off-axis phase-shifting electron holography, Appl. Phys. Lett. 89 (2006) 244101.
[126] S. Anada, K. Yamamoto, H. Sasaki, N. Shibata, Y. Hori, K. Kinugawa, A. Imamura, T. Hirayama, Precise measurement of electric potential, field, and charge density profiles across a biased GaAs p-n tunnel junction by *in situ* phase-shifting electron holography, J. Appl. Phys. 122 (2017) 225702.
[127] C.T. Koch, Towards full-resolution inline electron holography, Micron 63 (2014) 69–75.
[128] K. Song, S. Ryu, H. Lee, T.R. Paudel, C.T. Koch, B. Park, J.K. Lee, S.Y. Choi, Y.M. Kim, J.C. Kim, H.Y. Jeong, M.S. Rzchowski, E.Y. Tsymbal, C.B. Eom, S.H. Oh, Direct imaging of the electron liquid at oxide interfaces, Nat. Nanotechnol. 13 (2018) 198.
[129] H. Lichte, F. Börrnert, A. Lenk, A. Lubk, F. Röder, J. Sickmann, S. Sturm, K. Vogel, D. Wolf, Electron holography for fields in solids: problems and progress, Ultramicroscopy 134 (2013) 126–134.
[130] A. Tonomura, Development of electron holography and its applications to fundamental problems in physics, Jap. J. Appl. Phys. 47 (2008) 11–18.
[131] D. Shindo, Y. Murakami, Electron holography study of electric field variations, J. Electron Microsc. 60 (S1) (2011) S225–S237.
[132] K. Yamamoto, T. Hirayama, T. Tanji, Development of advanced electron holographic techniques and application to industrial materials and devices, J. Electron Microsc. 62 (S1) (2013) S29–S41.